

Magnetic, structural, and transport properties of the Heusler alloys Co_2MnSi and NiMnSb

Lance Ritchie and Gang Xiao

Physics Department, Brown University, Providence, Rhode Island 02912, USA

Y. Ji, T. Y. Chen, and C. L. Chien

Physics Department, Johns Hopkins University, Baltimore, Maryland 21218, USA

Ming Zhang, Jinglan Chen, Zhuhong Liu, and Guangheng Wu

State Key Laboratory for Magnetism, Institute of Physics, Chinese Academy of Science, Beijing 100080, People's Republic of China

X. X. Zhang

Physics Department, Hong Kong University of Science and Technology, Kowloon, Hong Kong, China

(Received 18 June 2003; published 29 September 2003)

We report on structural, magnetic, transport, and spin-polarization measurements of the Heusler alloys Co_2MnSi and NiMnSb . Laue diffraction patterns confirm the single-crystal nature of Co_2MnSi . Room-temperature transport measurements show a negative magnetoresistance in NiMnSb . Point-contact Andreev reflection measurements of the spin polarization yield polarization values for Co_2MnSi and NiMnSb of 56% and 45%, respectively. Temperature dependence of resistivity for Co_2MnSi reveals a relatively large residual resistivity ratio ($\rho_{293\text{ K}}/\rho_{5\text{ K}}$) typical of single-crystal Heusler alloys. In NiMnSb , resistivity and magnetization as a function of temperature show evidence of a magnetic phase transition near 90 K.

DOI: 10.1103/PhysRevB.68.104430

PACS number(s): 75.50.Cc, 72.15.Eb, 72.25.Ba, 75.60.Ej

I. INTRODUCTION

The increasing interest in materials with high-spin polarization derives largely from their proposed use as elements in multilayered magnetoelectronic devices such as the magnetic tunnel junction^{1,2} and the giant magnetoresistance spin valve.³ Because magnetoresistance of the multilayer device is due to the parallel versus antiparallel configurations of moments on adjacent ferromagnetic layers, magnetoresistance (MR) is ultimately limited by the spin polarization of the ferromagnetic elements. The Fe-, Co-, and Ni-based electrodes which are currently used in MR devices have a spin polarization of $\sim 45\%$,⁴ which provides for an optimal MR of $\sim 50\%$. This optimal MR is seldom achieved due to imperfections introduced during device processing. In contrast, a perfectly spin-polarized material (i.e., $P=100\%$) would allow no current to flow in the antiparallel configuration, leading to an infinitely large optimal MR.

Electronic band-structure calculations have predicted the existence of materials, called half metals, with $P=100\%$.⁵ Notable among the half metallic candidates are a number of the Heusler ($L2_1$ structure) and half Heusler ($C1_b$ structure) alloys.^{5,6} The Heusler alloy Co_2MnSi and the half Heusler alloy NiMnSb are especially promising device candidates due to their large minority-spin band gaps of $\sim .5$ eV (Refs. 7 and 8) and their high Curie temperatures of 985 K (Ref. 9) and 728 K,¹⁰ respectively. In this paper, we present a study of basic structural, magnetic, and transport properties of NiMnSb and single-crystal Co_2MnSi . Measurements of the spin polarization by the point-contact Andreev reflection (PCAR) technique are also presented and discussed.

II. CRYSTAL GROWTH AND CHARACTERIZATION

For the samples studied in this paper, boules of Co_2MnSi and NiMnSb were grown by the Czochralski method in a

Crystalox MCGS-3 cold crucible system using constituent elements (Co, Mn, Si, Ni, and Sb) having a purity of 99.95%. A 20-mm/hr growth rate and a 30-rpm rotation rate were used for the growth process. Slicing the boules perpendicular to the growth axis yielded disk-shaped samples, which were then prepared for Laue diffraction imaging using ultrafine metallographic sanding papers.

The resulting Laue image for Co_2MnSi which is shown in Fig. 1(a) clearly demonstrates the expected fourfold symmetry about the $[100]$ crystal axis. Laue diffraction images were generated for a series of points across the face of one of the Co_2MnSi disks, yielding identical diffraction patterns and confirming the single-crystal nature of our sample. Figure 1(b) is a photographic image of the original single-crystal Co_2MnSi boule. Analysis of a Laue diffraction image gener-

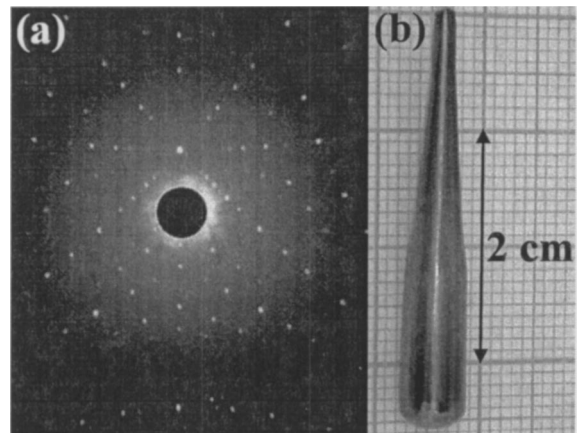


FIG. 1. (a) Laue diffraction pattern of single-crystal Co_2MnSi generated with the beam axis coincident with the crystal-growth axis. (b) Photographic image of single-crystal Co_2MnSi boule.

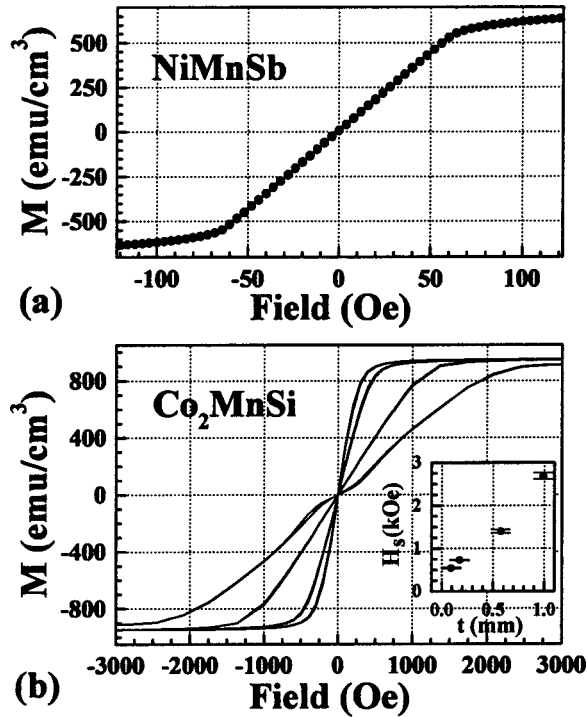


FIG. 2. (a) Magnetic hysteresis loop measured at 140 K for a NiMnSb sample with large aspect ratio ($L/A^{1/2}=19.0$) and length axis parallel to the field axis. (b) Four magnetic hysteresis loops measured at 293 K for a 3-mm Co_2MnSi disk with the disk axis perpendicular to the field axis. The four loops correspond to four thicknesses of the 3-mm disk. Inset graph shows saturation magnetic field (H_s) as a function of disk thickness (t).

ated with the sample face perpendicular to the x-ray beam reveals that the crystal-growth axis is not perpendicular to any low index plane. An identical x-ray analysis was carried out for the NiMnSb sample. Although single Laue images of the NiMnSb appear as single crystal for the 1-mm x-ray spot size, the series of images probing the extent of the disk face revealed a distinct shift of crystal orientation at one point along the face, suggesting that the NiMnSb boule was composed of several large grains. Despite the multigrained nature of the NiMnSb sample, we believe that, given the very small contact area utilized by the PCAR technique, our sample may be considered single crystal for the purpose of such measurements.

III. MAGNETIC PROPERTIES

Magnetic hysteresis curves were measured for a variety of sample geometries at 5 K and 293 K for applied fields to 3 T. A representative $M(H)$ loop is shown in Fig. 2(a). For every $M(H)$ loop measured, the remanence was zero, and the saturation field was completely determined by shape-dependent demagnetization effects. $M(H)$ curves with small saturation field ($H_s < 1000$ Oe) were typically characterized by a sharp approach to saturation, with the bulk of the unsaturated region remaining very linear. Figure 2(b) shows a series of $M(H)$ curves for a single disk-shaped sample oriented with the disk axis perpendicular to the field axis. The sample

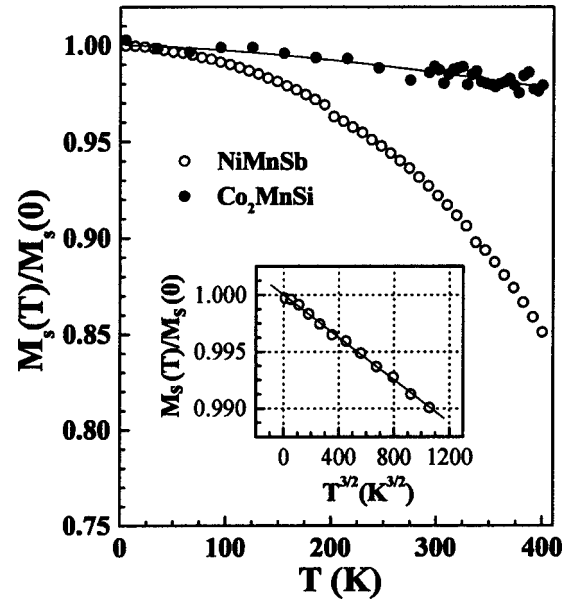


FIG. 3. Temperature dependence of the saturation magnetization for NiMnSb and Co_2MnSi . Magnetization is normalized to the 0-K magnetization as extrapolated from the fitted curves. The solid line is a $T^{3/2}$ fit to the Co_2MnSi data. Inset graph shows the NiMnSb data for $T < 100$ K as a function of $T^{3/2}$. The solid line in the inset graph is a linear fit to the NiMnSb data, demonstrating the $T^{3/2}$ dependence of the magnetization for this low- T range.

thickness was systematically varied to generate the family of curves. As the sample was ground to smaller thicknesses, diminished demagnetization forces allowed for saturation at a lower applied field. The saturation magnetic moments at 5 K for NiMnSb and Co_2MnSi were measured to be $4.02\mu_B$ per f.u. and $4.78\mu_B$ per f.u., respectively. Our results compare favorably with predicted theoretical integral values of $4\mu_B$ per f.u. for NiMnSb (Ref. 11) and $5\mu_B$ per f.u. for Co_2MnSi .⁷ All magnetic measurements were performed using a Quantum Design superconducting quantum interference device magnetometer.

Saturation magnetization as a function of temperature was measured over the range 5–400 K. The saturation magnetization $M(T)$ curves are shown in Fig. 3. Spin-wave theory predicts that, at low T , the magnetization curves should follow the functional form $M(T) = M(0)(1 - AT^n)$ with $n = 1.5$. Fitting the data for Co_2MnSi to this functional form yields a best-fit value for n of 1.41 ± 0.32 , while letting n be fixed at the theoretical value 1.5 yields a best-fit value for A of $2.81 \pm 0.21 \times 10^{-6} \text{ K}^{-3/2}$. The $n = 1.5$ fit is included in Fig. 3.

The spin-wave stiffness coefficient D from the spin-wave dispersion relation $\hbar\omega = Dq^2$ may be calculated from the parameter A via the relation $A = 2.612(V/S)(k_B/4\pi D)^{3/2}$ where V is the volume per magnetic atom and S is the spin.¹² Calculation for Co_2MnSi gives the value $D = 466 \text{ meV \AA}^2$. For NiMnSb, $n = 1.5$ allows for an excellent fit to the data for the low-temperature range 5–100 K. This fit, shown in the inset of Fig. 3, yields a value for A of $9.31 \pm 0.16 \times 10^{-6} \text{ K}^{-3/2}$, and a corresponding value for D of 255 meV \AA^2 . Above 100 K, our data for NiMnSb does not conform to the Bloch $T^{3/2}$

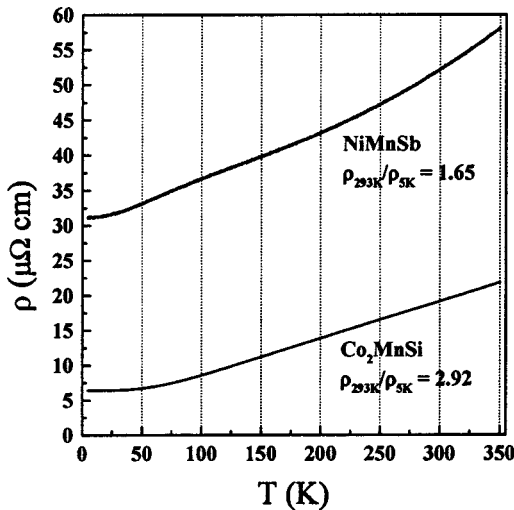


FIG. 4. Temperature dependence of the electrical resistivity for NiMnSb and Co₂MnSi. The small hump in the resistivity curve for NiMnSb (centered at 90 K) is consistent with a phase transition from half metallic ferromagnet to normal ferromagnet. The small residual resistivity (ρ_{5K}) for the Co₂MnSi sample indicates a good single-crystal Heusler structure.

law; instead we find best-fit values for $n \sim 1.9$ – 2.2 . The shift to an approximately quadratic temperature dependence has been seen by others in both thin-film¹³ and bulk single-crystal samples,¹⁴ and is attributed to a moment-ordering phase transition.

IV. ELECTRICAL TRANSPORT PROPERTIES

Electrical transport measurements were performed in a Quantum Design MPMS, which allows for temperature control over the range 2.3–400 K, and applied fields as great as 5.5 T. Long rodlike samples with large aspect ratio and length axis parallel to the crystal-growth axis were used for all transport measurements. Measurements utilized a standard four-point arrangement, with current flow parallel to the crystal-growth axis. To increase absolute resistance and thus minimize the influence of background μV fluctuations on our voltage measurements, the samples were first ground thin along a plane parallel to the length axis using standard metallographic grinding papers. Typical absolute resistances were of the order of $10^{-2} \Omega$. Sample contacts were made by manual bond using an In solder.

The resistivity ρ as a function of temperature is shown in Fig. 4. A significant degree of atomic disorder may be inferred from the large residual resistivity (ρ_{5K}) of our NiMnSb sample. The second derivative of the $\rho(T)$ curve for NiMnSb is positive at both high and low T , but becomes negative for $60 K < T < 120 K$. This transition of the second derivative is reflected in the humplike feature of the $\rho(T)$ curve centered at $\sim 90 K$. A similar shift in the temperature dependence of the resistivity of single-crystal NiMnSb was documented in an earlier paper.¹⁵ In that paper, Borca *et al.* provided evidence of a magnetic phase transition between 80 and 100 K. The observed power-law shift may be attributed to this phase transition. For Co₂MnSi, $\rho_{5K} \sim 7 \mu\Omega \text{ cm}$ com-

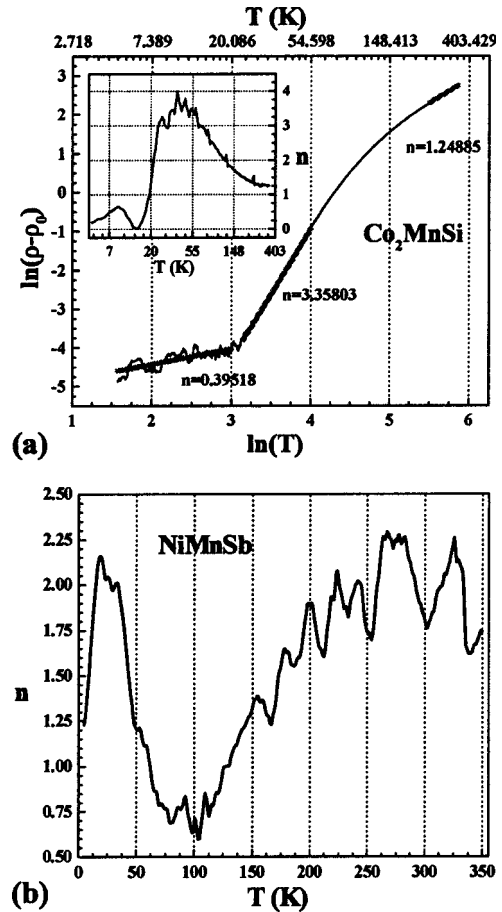


FIG. 5. (a) $\ln(\rho - \rho_0)$ as a function of $\ln(T)$ for the Co₂MnSi resistivity data. The slope of this curve corresponds to the power-law exponent n if we assume the functional form $\rho(T) = \rho_0 + cT^n$. The three distinct ranges of linearity are designated by the thick shaded lines, and labeled with the corresponding power-law exponent. The inset graph shows the power-law exponent as a continuous function of T . (b) The power-law exponent n plotted as a continuous function of T for the NiMnSb resistivity data, assuming the functional form $\rho(T) = \rho_0 + cT^n$.

pares favorably with earlier measurements of single-crystal specimens.^{16,17} The residual resistivity ratio $\rho_{293K}/\rho_{5K} \sim 3$, which is large for Co₂MnSi, corresponds to a relatively small contribution to the resistivity from lattice defects and other forms of atomic disorder. We point to this residual resistivity ratio as further evidence of a single-crystal structure.

An analysis of the resistivity data for Co₂MnSi is given in Fig. 5(a). By assuming the functional form $\rho = \rho_0 + cT^n$ for our data, a plot of $\ln(\rho - \rho_0)$ as a function of $\ln(T)$ will yield a curve whose slope corresponds to the local power-law parameter n . Our analysis shows ρ to be nearly constant for $T < 22 K$ and nearly linear for $T > 150 K$. The inset of Fig. 5(a) shows the variation of n as a function of T . In the critical low- T region $22 K < T < 65 K$, the resistivity behaves according to $a \sim T^3$ power law. For $65 K < T < 150 K$, the dependence transitions smoothly from a T^3 dependence to an almost purely phononic linear dependence. This power-law trend typifies the Bloch-Grüneisen formula, and suggests a

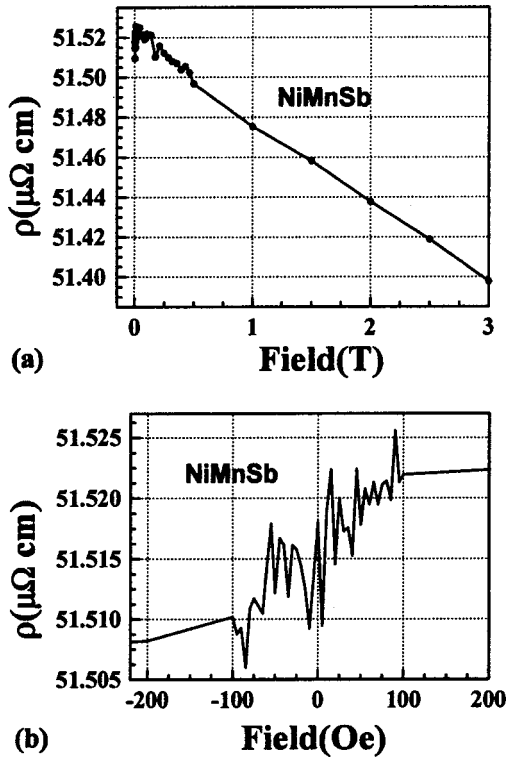


FIG. 6. (a) The longitudinal magnetoresistance data for NiMnSb at 293 K. The change in resistivity for the high-field measurements (>0.5 T) corresponds to a negative magnetoresistance of $0.076\%/T$. (b) The low-field longitudinal magnetoresistance data for NiMnSb at 293 K. The change in resistivity over the range $-100 \text{ Oe} < H < 100 \text{ Oe}$ corresponds to a very small anisotropic magnetoresistance of $\sim 0.023\%$.

dominance of phonon scattering in this temperature range. A similar power-law analysis for NiMnSb resistivity is detailed in Fig. 5(b). Here, the 90-K phase transition is seen as a dramatic decline of the local power-law exponent. Our resistivity data shows that, aside from this transition, NiMnSb behaves like an ordinary ferromagnetic material, with $n=2$ for temperatures both below and above the transition region.

To probe the magnetoresistive characteristics of our samples, resistance as a function of magnetic field was measured for fields up to 3 T. For our measurements, the field axis coincides with both the crystal-growth axis and current flow. Magnetoresistance data for NiMnSb is shown in Fig. 6(a). In the magnetically saturated region, $H > 100$ Oe, we observe a negative isotropic magnetoresistance. Over the range $0.5\text{--}3$ T, we find $d\rho/\rho_0 = 0.076\%/T$. This value for the longitudinal magnetoresistance at 293 K compares favorably to the earlier results of Borca *et al.*, who ascribed the negative magnetoresistance to the opening of a spin-flip scattering channel above the moment-ordering transition.¹⁵ Figure 6(b) gives a detailed view of the $R(H)$ curve for NiMnSb at low fields. In this unsaturated region, $-100 \text{ Oe} < H < 100 \text{ Oe}$, we observe a very small anisotropic magnetoresistance of $\sim 0.023\%$. For Co_2MnSi , no magnetoresistance was observed to within the limits of our measurement system.

V. SPIN POLARIZATION

The spin polarization for both samples was measured at 4.2 K using the point-contact Andreev reflection (PCAR) technique. The PCAR technique involves measurement of the conductance through a superconducting point contact and into the metal being tested.

The conversion of supercurrent to normal current at the superconductor/metal interface, called Andreev reflection, is limited by the carrier density of the minority-spin band at the Fermi level in the metal. In the case of a spin-polarized metal, the imbalance between majority-spin and minority-spin conduction electrons leads to a suppression of Andreev reflection. For voltages smaller than the superconducting gap, conductance can only occur by means of Andreev reflection. Thus, the spin polarization (P) of the metal may ideally be determined by analyzing the PCAR conductance curve.

In the limit of a perfectly clean ballistic contact, it can be shown that $G_0/G_n = 2(1-P)$ where G_0 is the conductance at zero bias and G_n is the conductance at high bias. The requirement of a ballistic contact presents an engineering challenge with respect to the fabrication of the point contact, since the dimensions of the contact area must necessarily be small compared to the mean-free-electron path in the metal being tested. In most any real world PCAR measurement, a Fermi velocity mismatch and/or oxide layer will result in some barrier at the contact interface. Since the reflection of current by the barrier will influence the conductance curve, it is necessary to analyze the conductance curve using a model that takes into account the nonideal contact conditions. For this paper, the PCAR conductance curves were analyzed using a modified Blonder-Tinkham-Klapwijk model.^{18,19}

Representative PCAR conductance curves for Co_2MnSi and NiMnSb are given in Fig. 7. Using a Nb point contact, theoretical fits to the PCAR conductance curves for Co_2MnSi yield a value for spin polarization P of $\sim 55\%$. This value agrees with the recent measurement of P in Co_2MnSi by Cheng *et al.*¹⁶ A Nb point contact was also used for the PCAR measurements of NiMnSb. Our fits to the NiMnSb conductance curves yield a P of only $\sim 45\%$. This is markedly lower than previously reported P measurements of $50\%\text{--}60\%$.^{4,20} In the model by Mazin *et al.*,¹⁹ interfacial scattering is represented by a delta function potential characterized by a barrier strength parameter (Z). Conductance analysis uses Z , P , and the Nb superconducting gap as fit parameters, while temperature is fixed at 4.2 K. For our NiMnSb sample, we extract Z values in the range $0\text{--}0.4$, while for the Co_2MnSi sample, fit values for Z are always very near zero.

Although both NiMnSb and Co_2MnSi have been predicted to be half metallic, spin-polarization measurements thus far have failed to show half metallic nature. Several authors have pointed to surface segregation and surface electronic structure to explain the lackluster P values. In NiMnSb, for example, extensive Mn surface segregation has been observed.²¹ In another paper, this same group established a strong sensitivity of spin-polarized inverse photoemission measurements to the surface preparation of

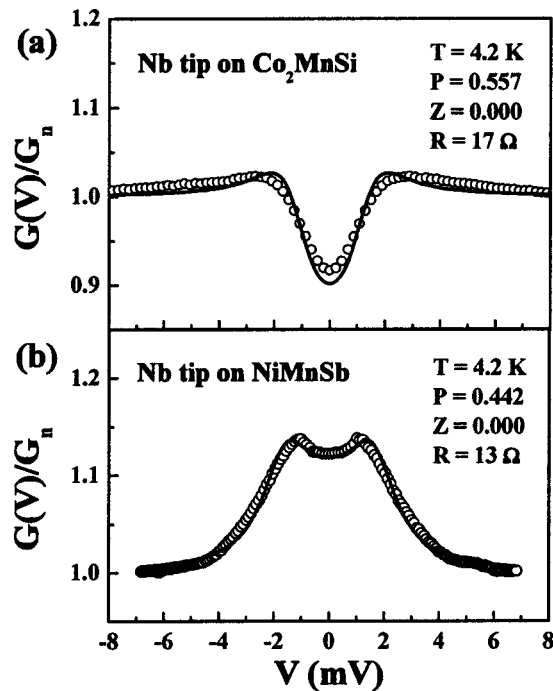


FIG. 7. Conductance versus voltage curves using a Nb point contact at 4.2 K. In each graph, the corresponding spin polarization (P), contact resistance (R), and barrier strength (Z) are indicated. The solid line is a theoretical fit to the data using a modified Blonder-Tinkham-Klapwijk model.

NiMnSb.²² Polarization measurements of the Heusler alloys are also likely to suffer as a result of antisite disorder. In NiMnSb, for example, it has been shown that atomic disorder will degrade the spin polarization through the introduction of states in the minority-spin band gap.²³

In the case of Co_2MnSi , antisite disorder is manifested in the form of site swapping between the Co and Mn atoms. The similar atomic radii of the Co and Mn atoms encourages this kind of disorder, and a recent study, using x-ray-absorption fine-structure measurements and neutron diffraction to probe the disorder of Co_2MnSi , shows $\sim 7\%$ Co-Mn site swapping.²⁴

The disorder of NiMnSb can be explained by the Heusler

structure, which is that of four interpenetrating fcc lattices. For the $C1_b$ structure of NiMnSb, one of these fcc lattices should be empty. And so, in addition to Ni-Mn site swapping, occupancy of the vacant sublattice will also contribute to the antisite disorder. Orgassa *et al.* calculated the effects of three types of antisite disorder, and predicted a significant reduction of spin polarization resulting from disorder levels of only a few percent.²⁵ An experimental study of the similar half Heusler PtMnSb finds an appreciable disorder of $\sim 10\%$.²⁶ We note that even if atomic disorder can be eliminated, there is, as previously mentioned, considerable evidence of a phase transition to a normal ferromagnetic state near 90 K. Thus, NiMnSb may ultimately be limited to low-temperature applications.

VI. SUMMARY

In conclusion, our temperature-dependent measurements of both magnetization and resistivity of NiMnSb support the theory of a phase transition at 80–100 K. We record a small negative longitudinal magnetoresistance for NiMnSb of 0.076%/T at high field, and see evidence of a small anisotropic MR in the unsaturated low-field range. Despite the verification via Laue diffraction of single crystallinity on a macroscopic scale, our measurements of a spin polarization of $\sim 45\%$ for NiMnSb are relatively low, and do not indicate a half metal. For our Co_2MnSi sample, we verify the single-crystal nature via Laue diffraction and find a low residual resistivity of $\sim 7 \mu\Omega \text{ cm}$; its spin polarization of $\sim 55\%$ falls short of half metallic, but is higher than the polarization of more common ferromagnets such as Fe, Ni, and Co. We suspect that surface effects (e.g., surface segregation) and antisite disorder are the causes of diminished spin polarization.

ACKNOWLEDGMENTS

This work is partially supported by the National Science Foundation, Grant Nos. DMR-0306711 and DMR-0080031. X.X. Zhang and G.H. Wu wish to acknowledge financial support of Hong Kong RGC Grant No. HKUST6059/02E.

¹M. Julliere, Phys. Lett. **54A**, 225 (1975).

²J.S. Moodera, L.R. Kinder, T.M. Wong, and R. Meservey, Phys. Rev. Lett. **74**, 3273 (1995).

³B. Dieny, V.S. Speriosu, S.S.P. Parkin, B.A. Gurney, D.R. Wilhoit, and D. Mauri, Phys. Rev. B **43**, 1297 (1991).

⁴R.J. Soulen, J.M. Byers, M.S. Osofsky, B. Nadgorny, T. Ambrose, S.F. Cheng, P.R. Broussard, C.T. Tanaka, J. Nowak, J.S. Moodera, A. Barry, and M.D. Coey, Science **282**, 5386 (1998).

⁵R.A. de Groot, F.M. Mueller, P.G. van Engen, and K.H.J. Buschow, Phys. Rev. Lett. **50**, 2024 (1983).

⁶S. Ishida, T. Masaki, S. Fujii, and S. Asano, Physica B **245**, 1 (1998).

⁷S. Fujii, S. Sugimura, S. Ishida, and S. Asano, J. Phys.: Condens. Matter **2**, 8583 (1990).

⁸J.-S. Kang, J.-G. Park, C.G. Olson, S.J. Youn, and B.I. Min, J. Phys.: Condens. Matter **7**, 3789 (1995).

⁹P.J. Brown, K.U. Neumann, P.J. Webster, and K.R.A. Ziebeck, J. Phys.: Condens. Matter **12**, 1827 (2000).

¹⁰M.J. Otto, R.A.M. van Woerden, P.J. van der Valk, J. Wijngaard, C.F. van Bruggen, C. Hass, and K.H.J. Buschow, J. Phys.: Condens. Matter **1**, 2341 (1989).

¹¹R.B. Helmholtz, R.A. de Groot, F.M. Mueller, P.G. van Engen, and K.H.J. Buschow, J. Magn. Magn. Mater. **43**, 249 (1984).

¹²W. Marshall and S. Lovesey, *Theory of Thermal Neutron Scattering* (Clarendon, Oxford, 1971).

¹³D. Ristoiu, J.P. Nozieres, and L. Ranno, J. Magn. Magn. Mater. **219**, 97 (2000).

- ¹⁴C. Hordequin, J. Pierre, and R. Currat, *J. Magn. Magn. Mater.* **162**, 75 (1996).
- ¹⁵C.N. Borca, T. Komesu, H.-K. Jeong, P.A. Dowben, D. Ristoiu, C. Hordequin, J.P. Nozieres, J. Pierre, S. Stadler, and Y.U. Idzherda, *Phys. Rev. B* **64**, 052409 (2001).
- ¹⁶S.F. Cheng, B. Nadgorny, K. Bussmann, E.E. Carpenter, B.N. Das, G. Trotter, M.P. Raphael, and V.G. Harris, *IEEE Trans. Magn.* **37**, 2176 (2001).
- ¹⁷M.P. Raphael, B. Ravel, M.A. Willard, S.F. Cheng, B.N. Das, R.M. Stroud, K.M. Bussmann, J.H. Claassen, and V.G. Harris, *Appl. Phys. Lett.* **79**, 4396 (2001).
- ¹⁸G.E. Blonder, M. Tinkham, and T.M. Klapwijk, *Phys. Rev. B* **25**, 4515 (1982).
- ¹⁹I.I. Mazin, A.A. Golubov, and B. Nadgorny, *J. Appl. Phys.* **89**, 7576 (2001).
- ²⁰G.L. Bona, F. Meier, M. Taborelli, E. Bucher, and P.H. Schmidt, *Solid State Commun.* **56**, 391 (1985).
- ²¹D. Ristoiu, J.P. Nozieres, C.N. Borca, B. Borca, and P.A. Dowben, *Appl. Phys. Lett.* **76**, 2349 (2000).
- ²²D. Ristoiu, J.P. Nozieres, C.N. Borca, T. Komesu, H.-K. Jeong, and P.A. Dowben, *Europhys. Lett.* **49**, 624 (2000).
- ²³H. Ebert and G. Schütz, *J. Appl. Phys.* **69**, 4627 (1991).
- ²⁴B. Ravel, M.P. Raphael, V.G. Harris, and Q. Huang, *Phys. Rev. B* **65**, 184431 (2001).
- ²⁵D. Orgassa, H. Fujiwara, T.C. Schulthess, and W.H. Butler, *Phys. Rev. B* **60**, 13 237 (1999).
- ²⁶M.C. Kautzky, F.B. Mancoff, J.F. Bobo, P.R. Johnson, R.L. White, and B.M. Clemens, *J. Appl. Phys.* **81**, 4026 (1997).